The effect of Zn on precipitation in Al-Mg-Si alloys

Takeshi Saito[1,*], Sigurd Wenner[1,a], Elisa Osmundsen[1,b], Calin D. Marioara[2,c], Sigmund J. Andersen[2,d], Jostein Røyset[3,e], Williams Lefebvre[4,f] and Randi Holmestad[1,g]

[1]*Department of Physics, Norwegian University of Science and Technology (NTNU), N-7491 Trondheim, Norway*

[2]*SINTEF Materials and Chemistry, N-7465 Trondheim, Norway,*

[3]*Hydro Aluminum Research and Technology Development, N-6601 Sunndalsøra, Norway*

[4]*Université de Rouen, GPM, UMR CNRS 6634 BP 12, Avenue de I'Université, 76801 Saint Etienne du Rouvray, France*

* Corresponding author

Email: takeshi.saito@ntnu.no

Telephone: + 47 73 59 07 30

Fax: +47 73 59 77 10

[a]sigurd.wenner@ntnu.no, [b]elisaosmundsen@gmail.com, [c]calin.d.marioara@sintef.no, [d]sigmund.j.andersen@sintef.no, [e]jostein.royset@hydro.com, [f]williams.lefebvre@univ-rouen.fr, [g]randi.holmestad@ntnu.no

The effect of Zn on precipitation in Al-Mg-Si alloys

Effects of Zn additions (up to 1 wt%) on microstructure, precipitate structure and intergranular corrosion (IGC) in an Al-Mg-Si alloys was investigated. During aging at 185°C, the alloys showed modest increases in hardness as function of Zn content, corresponding to increased number densities of needle-shaped precipitates in the Al-Mg-Si alloy system. No precipitates of the Al-Zn-Mg alloy system were found. Using high angle annular dark-field scanning transmission electron microscopy (HAADF-STEM), the Zn atoms were incorporated in the precipitate structures at different atomic sites with various atomic columns occupancies. Zn atoms segregated along grain boundaries, forming continuous film. It correlates to high intergranular corrosion (IGC) susceptibility when Zn concentration is ~1wt% and the materials in peak-aged condition.

1. Introduction

1.1. Al-Mg-Si alloys

The 6xxx series aluminum alloys (i.e. Al-Mg-Si alloy system) constitute an important heat-treatable alloy system. They are used in a wide range of industrial applications since they have advantageous properties: high strength-weight ratio, good formability and corrosion resistance. Their main feature is an increase in hardness during a final isothermal heat treatment (i.e. artificial aging) at an adequate temperature and time. During the artificial aging, a large number of various nano-sized semi-coherent metastable precipitates will form. These precipitates set up surrounding strain fields which prevent dislocation movement due to the interfacial strain into the aluminum matrix (i.e. precipitation hardening). The interfacial strain depends on atomic matching at the precipitate/matrix interface. Hence the alloy properties depend ultimately on the

precipitate types and the microstructure they produce (sizes, numbers and orientations). The precipitation sequence comprises several metastable precipitates. The metastable precipitates form as a consequence of precipitation which is controlled by the alloy composition and thermo-mechanical history. The precipitation sequence of the Al-Mg-Si alloys is as follows: [1-8]:

SSSS → atomic clusters → GP zones (pre-β") → β"→ β', U1, U2, B' → β, Si

where SSSS stands for super saturated solid solution. Solute elements become supersaturated in the fcc Al lattice after rapid cooling from a solution heat treatment to room temperature. The diffusion of the solute elements starts even at room temperature leading to nucleation of the atomic clusters. The atomic clusters grow rapidly into metastable precipitates during the artificial aging. Fully coherent Guinier - Preston (GP) zones form initially with the solute elements occupying fcc positions in the Al matrix. The subsequent metastable precipitates are seen to keep the alignment of some planes (fully coherent) only in one direction, corresponding to <001>Al which is the main growth direction of the precipitates. As a consequence, they have needle/lath/rod morphologies extending along <001>Al directions. The main hardening precipitates are the highly-coherent, needle-shaped GP zones and β" phase which form the finest microstructures, characterized by large number densities of small (short, thin) needles. The U1, U2 and B' (also known as Type-A, Type-B and Type-C, respectively [9].) are larger, thicker needles/rods/laths. They mostly form together with β' (rod) upon over-aging. They are semi-coherent and produce coarse microstructures with low strength. The equilibrium β (Mg2Si) phase is incoherent and can be both plates or cube-shaped. It

forms and grows rapidly at higher temperatures and Mg content. It often coexists with pure Si particles with diamond structure, depending on the Si content of alloy.

1.2. Effects of additional alloying elements

Effects of additional alloying elements in the Al-Mg-Si alloys are of key interest since they affect directly the microstructure and precipitate structure. For instance, Cu (~0.4 wt%) drastically alters the precipitation sequence as follows [10-14]:

$$SSSS \rightarrow \text{atomic clusters} \rightarrow \text{GP zones} \rightarrow \beta", L, S, C, QP, QC \rightarrow \beta', Q' \rightarrow Q.$$
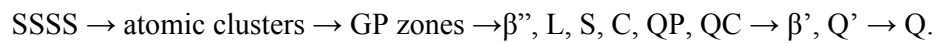
The proportion of the β" phase diminishes strongly for increased Cu content. The other metastable precipitates such as L, S, C, QP and QC form at peak-aged conditions [10, 11]. The Q' phase forms in over-aged conditions [10, 12]. Q' is most likely isostructural to the equilibrium Q phase [14].

An interesting feature of the Al-Mg-Si-(Cu) alloy system is that all metastable precipitates, as well as the equilibrium Q phase, are structurally connected through a common network of Si atomic columns (Si-network) with a projected near hexagonal symmetry of a = b ≈ 0.4 nm, c = n × 0.405 nm (n is integer), with c parallel to the needle/rod/lath main growth directions [7, 10]. Consequently, the precipitates consist of different arrangements of Al, Mg and Cu atomic columns located in-between the Si-network columns. Typically Cu promotes the formation of disordered precipitates, which lack a unit cell, although they are based on the Si-network. In the β" phase, the Si-network is distorted, probably because of its highly coherency with the Al matrix.

Ge is another additional alloying element influencing precipitation in the Al-Mg-Si(-Cu) alloys. It leads to the formation of Ge containing hardening phases which

are isostructural with the β' and U1 phases in the Al-Mg-Si alloy system [15-17]. It was found that Ge forms a network similar to the Si-network. It is mixed (Si/Ge) when both elements are present in the alloy [17].

Additions of Ag (~0.5 wt%) in the Al-Mg-Si alloy system lead to an increase in hardness and elongation [18] by means of a new Ag containing phase, called β'Ag phase where Ag replaces one third of the Si-network columns [19].

The amount of these additional alloying elements is an important factor influencing alloy properties and precipitation. It was previously demonstrated [20] that a low addition of Cu (~0.1 wt%) leads to a higher number density of precipitates, and consequently to higher strength, although the precipitation sequence is not altered. Furthermore, this level of Cu makes the β" precipitates partially disordered in the same precipitate needle, which is also structurally connected to the Si-network [20]. A low additions of Ca (~0.1 wt.%) lowers, on the other hand, the precipitate number density, because of formation of large Ca-containing particles which absorb Si [21].

1.3. Zn as an additional alloying element

Zn is the main alloying element in the heat-treatable 7xxx series (Al-Zn-Mg) aluminum alloys. For instance, the commercial 7075 alloy typically contains 5.5Zn, 2.5Mg and 1.5Cu (wt%). In this system, Zn atoms combine with Mg to form plate-like semi-coherent η' metastable precipitates and equilibrium η-MgZn2 precipitates on {111}Al planes [22-24]. These alloys have very low Si content. Our interest here is to investigate how modest additions of Zn influence Al-Mg-Si alloys. Concurrently, recycling of Al alloys is a noteworthy activity in the Al industry. Since Zn is one of the trace elements that can potentially be end up in aluminum scrap metals during recycling, it is important to know to which extent different levels of Zn will influence the microstructure, precipitate structure, mechanical and corrosion properties in Al-Mg-Si alloys. In the

present paper, influence of Zn on the precipitation in Al-Mg-Si alloys has systematically been investigated for different levels of Zn (up to 1wt%).

2. Experimental Procedure

Five alloys were prepared from ultrapure Al with different amounts of Zn (0.000, 0.001, 0.01, 0.1 and 1 wt.%). The levels of Mg and Si were fixed. The alloys were cast as cylindrical ingots with 95 mm in diameter, from which extrusion billets were cut. The alloy compositions were measured by inductively coupled plasma optical emission spectroscopy and are shown in Table 1. Hereafter the alloys with different amounts of Zn will be referred to as LZ0, LZ1, LZ2, LZ3 and LZ4 as shown in Table 1. All contain ~0.07wt% Fe, which is lower than for most industrial alloys. The billets were homogenized at 575°C for 2.5 hours and subsequently extruded into round profiles with 20 mm in diameter. The extrusions were conducted using a direct press and a single-hole die. The extrusion temperature was in the range 500-510°C, which is well above the solvus temperature for the alloys. The entire extruded profiles were water-quenched approximately 5 seconds after the die exit. Thus only a short solid solution heat treatment was needed prior to subsequent heat treatment procedures. The extruded profiles were cut into 500 mm lengths, solution heat treated in an air circulation oven at 540 °C for 1 hour, and subsequently water-quenched. The alloys were then exposed to room temperature (i.e. natural aging) for a total of 4 hours. Furthermore, the alloys were aged at 185°C in the air circulation oven.

Vickers hardness measurements were carried out along the extrusion direction on transversally cut slices. A Durascan-70 (Struers) machine was used for the hardness measurements. The hardness indenter carried a 5 kg load. The loading time was 15 seconds. Each data point corresponds to the average of ten hardness indentations, with the corresponding standard error. Electrical conductivity measurements were carried out

at room temperature on the same surface as the hardness measurements. A SIGMATEST 2.069 operated at a frequency of 960 kHz was used. Each data point corresponds to the average of five conductivity measurements, with the corresponding standard error. Calibration of the equipment for the conductivity measurement was performed regularly in order to minimize error of the measurements. The hardness and conductivity were measured on the samples at 17 different aging times up to 24 hours.

TEM specimens were prepared by electropolishing with a Tenupol 5 machine (Struers), on the transversal slices used in the hardness measurements. The electrolyte consisted of 1/3 HNO3 in methanol and the solution was kept at a temperature between -20 and -35°C. Precipitate microstructure was investigated by TEM in bright-field mode using a Philips CM30 operated at 150 kV with a double-tile holder. The thickness of the specimens was measured with a Gatan parallel electron energy loss spectrometer (PEELS). The thickness measurements were performed in the central area shown in the micrographs. The thickness of all images shown in this study is around 70 to 110 nm. All TEM and PEELS analyses were performed along <001>Al directions where approximately 1/3 of the needles can be viewed in cross-section and 2/3 perpendicular to the needle lengths. The combination of the TEM bright-field images and PEELS spectra enables average precipitate needle-lengths, cross-sections, number densities and volume fractions to be quantified. A full description of the methodology is given elsewhere [4, 25]. Precipitate atomic structures were investigated by high resolution high angle annular dark field scanning TEM (HAADF-STEM) using a spherical aberration (Cs) probe corrected JEOL ARM 200F STEM operated at 200 kV. The inner and outer collection angles of the HAADF detector were in the range of 45-150 mrad and the probe size was 0.1 nm. The HAADF-STEM technique enables to determine atomic column positions directly, being less affected by objective lens defocus and

specimen thickness compared to high resolution TEM. In addition, the technique

provides atomic number (Z) contrast with the intensity proportional to Z1.7-1.9 [26,

27]. This enables to distinguish the heavier Zn (ZZn = 30) atomic columns from those

of Mg (ZMg = 12), Al (ZAl = 13) and Si (ZSi = 14) in the precipitate structures. In

order to reduce contamination on the specimen during the HAADF-STEM observation,

all specimens were ion-milled in a precision ion polishing system (PIPS Gatan) and

further cleaned in plasma cleaner (SOLARUS, Gatan) before the observation. Fast

Fourier transform (FFT) filtering has been applied to the HAADF-STEM images in

order to reduce noise using a circular band pass mask which removes all periods shorter

than 0.15 nm. A JEOL 2010F operated at 200 kV and equipped with an energy

dispersive X-ray spectroscopy (EDS) from Oxford Instruments (with INCA software)

was used for elemental mapping. For these acquisitions, drift compensation was

activated, whereby the microscope regularly acquires annular dark field scanning TEM

(ADF-STEM) images and cross-correlates them to a reference image in order to adjust

the STEM-EDS scanning position.

Accelerated corrosion tests were performed by following the British Standard

(BS 11846 method B). The intergranular corrosion (IGC) susceptibility was evaluated

after the corrosion test. The samples for the corrosion test were cut from the round

extruded profiles parallel to the extrusion direction to a "D-shape" (a shape of half

cylinder) so that the metallography could be observed parallel with and perpendicular to

the extrusion direction. Before the corrosion test, the samples were degreased using

acetone and ethanol, followed by alkaline etching. The alkaline etching was conducted

with immersion in a 7.5 wt% NaOH solution for 3 minutes at 55-60°C, and then

desmutting in concentrated HNO3, which removed approximately 15 μm of sample

surface. The corrosion test was conducted by immersion for 24 hours in an acidified

soldium chloride solution (30g NaCl and 10 ml concentrated HCl per liter). After the immersion, the samples were washed in water and then in ethanol and subsequently dried. In order to investigate IGC susceptibility at different precipitation stages, samples with different heat treatment time were prepared corresponding to under-aged, peak-aged (T6) and over-aged (T7) conditions. Metallographic examinations after the corrosion test were conducted by optical microscopy.

3. Results and Discussion

3.1. Hardness and Electrical Conductivity

Figure 1 shows hardness and conductivity curves for the five Zn-containing alloys as a function of aging time, up to 24 hours. The observations from the curves can be explained as follows:

- Both hardness and conductivity increase with increasing aging time. This must be a result of precipitation; hardness increases as precipitates form, while conductivity increases since the Al matrix becomes depleted of solute atoms.

- The overall hardness of LZ4 is slightly higher than that for the other alloys while the conductivity is lower. Lower conductivity may indicate the presence of Zn in solid solution throughout the aging, while the slightly higher hardness could be due to the same effect (solution hardening), or in combination with a weak influence on precipitation. It is interesting to note that after 2 hours of aging time, corresponding to largest hardness difference between the alloys, hardness is nearly proportional with the Zn amount in the alloy. This indicates that Zn additions influence the formation of precipitates, although the effect seems to be weak.

- Interestingly the conductivity curves for LZ0 to LZ3 can be seen to converge with

increasing aging time. This could suggest that a certain amount of Zn diffuses from the Al matrix and enters into the precipitates. This phenomenon was not observed in LZ4, which may show that a saturation level of Zn in the precipitates has been reached.

3.2. Microstructure

Figure 2 shows bright-field TEM images for LZ1 and LZ4 after the aging at 185°C for 12 hours, representing peak-aged condition. The corresponding quantified microstructure parameters are summarized in Table 2. Only needle-like precipitates, typical for the Al-Mg-Si(-Cu) alloy system were observed along <100>Al directions. No plate-like precipitates were observed on {111}Al planes, as common for the Al-Zn-Mg alloy system. This indicates that η' or η phases do not formed in the investigated alloys. It should be noted that the normal aging temperatures in Al-Zn-Mg alloy system are lower (~120°C). It is therefore not impossible that these plate-like precipitates may form at the current aging temperature for the Al-Mg-Si alloys. Mg prefers to combine with Si to form needle-like precipitates, rather than with Zn for the composition and heat treatment given in this study. Homogeneous distributions of precipitates were observed for both alloys. The main difference between LZ1 and LZ4 is a slightly higher precipitate number density in LZ4, which correlates with a somewhat smaller precipitate average length and cross section, resulting in in the volume fraction. These results confirm, in the observations of hardness and conductivity, that Zn has a weak influence on precipitation, and consequently it should be expected that Zn is incorporated into the precipitate structure. This will be discussed in detail in a later sub-section.

Figure 3 shows an ADF-STEM image and corresponding to EDS elemental maps for relevant elements along a grain boundary and adjacent grains for the LZ4 after the aging at 185°C for 12 hours. The ADF-STEM contrast of precipitate needles can be

observed in the Al matrix, which clearly corresponds to the Mg and Si elemental maps.

A precipitate free zone can also be seen in the Mg and Si elemental maps in the vicinity

of the grain boundary. It is interesting to mention that EDS elemental map for Zn shows

a shape of a line indicating the presence of a Zn thin film along the whole grain

boundary. This continuous film can also be recognized in the contrast in the ADF-

STEM image. Figure 3 shows no trace of any precipitates in the Zn elemental map.

Quantitative analysis of EDS data indicates that the Zn concentration in the two grains

adjacent to the grain boundary is similar to the Zn nominal alloy composition. This

leads to the conclusion that Zn is homogeneously distributed in the Al matrix, which

seems to be supported by the observed low electrical conductivity of LZ4, see Figure

1(b). This supports that Zn can only exist in low amounts in the precipitate needles. If

Zn enters the composition of precipitate needles, it must be at a low level, below the

detectability limit of the EDS detector. The ADF-STEM contrast and elemental maps

along the grain boundary in Figure 3 also indicate formation of grain boundary

precipitates, consisting of Mg and Si. Based on EDS quantitative measurements, the

Mg/Si ratios for these precipitates was found to be 1.5~1.7, which seem to correspond

to the β' (Mg1.8Si) phase [6]. The data does not exclude the possibility of low Zn

amounts being incorporated into such grain boundary precipitates. One grain boundary

precipitate shows signals of Si and O, see Figure 3. In Al-Mg-Si alloys, it is not unusual

to find amorphous and/or oxidized remains. This is presumably attributed to damage

during electropolishing under specimen preparation.

3.3. Intergranular Corrosion (IGC) Susceptibility

As shown in the EDS elemental map, Zn segregates along grain boundaries at peak-

aged condition, forming an apparent continuous film. Among several types of corrosion

considered, IGC is of high interest since it is related to grain boundary precipitates and

atomic segregation on grain boundaries. In general, IGC is the result of microgalvanic reactions at grain boundaries; the grain boundary precipitates and/or segregated atoms are either active or noble with respect to the Al matrix. Figure 4 shows cross-section examinations after the IGC test for LZ3 and LZ4. Similar cross-section for the alloys with lower Zn contents; LZ0, LZ1 and LZ2 had strong resemblance with LZ3, thus showing negligible IGC susceptibility. This implies that levels of Zn below 0.1 wt% have little influence concerning IGC. On the contrary, the cross-section of LZ4 shows strong evidence of corrosion attacks, indicating that the IGC susceptibility is pronounced only for the highest Zn concentration (1 wt%). This indicates that the critical level of Zn to influence the IGC is somewhere between 0.1 and 1 wt%. It is interesting to note that the IGC susceptibility depends highly on heat treatment, being pronounced at peak-aged and over-aged conditions, as compared to an under-aged condition, see Figure 4. The results of the IGC susceptibility and the TEM investigations suggest that the observed difference in the IGC must somehow be related to the characteristics of the Zn thin film presenting along the grain boundaries for the high Zn content. This should be compared with a recent finding in Cu-containing Al-Mg-Si alloys. Here, IGC susceptibility was found to be reduced at peak-aged and over-aged conditions, when an analogous Cu-rich film along grain boundaries had become discontinuous during coarsening of grain boundary precipitates [28, 29]. Note that the results in the present study may be interpreted oppositely, since the IGC susceptibility increases at peak-aged and over-aged conditions with the Zn film. Our investigation also shows that the IGC susceptibility is dependent on the extrusion direction; the corrosion attacks were pronounced along the extrusion direction, compared to perpendicular to it, see Figure 4. This might be attributed to different grain boundary orientation and/or a fibrous texture along the extrusion direction.

3.4. Precipitate Structures

Based on the findings discussed in the previous sub-sections, it is still questionable whether or not Zn incorporates into the precipitate structure; the microstructure quantification (Table 2) shows that there is a correlation between an increased precipitate number density and a high Zn amount in the alloy composition, while the EDS maps (Figure 3) do not seem to show any Zn signal associated with the precipitates. In this sub-section, precipitate structure will be discussed by observations from aberration corrected HAADF-STEM. All HAADF-STEM images shown in this sub-section were taken from LZ4 after aging for 12 hours (peak-aged). They were taken from the <001>Al zone axis, corresponding to the cross sections of the precipitate needles. Owing to the high resolution of aberration-corrected HAADF-STEM, all atomic columns could be resolved in the structures. Based on the high Z contrast, a column having a sufficient fraction of Zn atom can easily be identified even in the unprocessed HAADF-STEM images. After filtering the images, weaker-contrast Si, Al and Mg atomic columns could also be resolved. The atomic overlays for all figures in this sub-section were based on the Z contrast, inter-atomic distances and local similarities with well-known structures in the Al-Mg-Si(-Cu) alloy system.

Most analyzed precipitates had disordered structures lacking a unit cell, but it was found that they still were based on the Si-network. Figures 5 to 7 show examples of disordered precipitates while Figure 8 displays a β" precipitate. A legend in Figure 9 explains the atomic overlays in Figures 5, 7 and 8, as well as unit cells of phases in which fragments are frequently encountered in the structure of the disordered precipitates. In the HAADF-STEM images, bright spots represent atomic columns containing Zn. This is a strong indication of the Zn incorporation into precipitates. In the disordered precipitates, the intensity of the Zn-containing columns in the disordered

precipitates was found to vary, indicating fluctuating, partial Zn occupancy. It is worth noting that the disordered precipitates were still based on a regular Si-network. They are found to contain fragments of known precipitates in the Al-Mg-Si(-Cu) system. As a consequence of the disorder, the Zn distribution is non-periodic. Columns containing Zn were identified both in-between the columns of the Si-network, as well as replacing Si network columns. In this respect, the Zn distribution resembles that of Cu [31] in similarly disordered precipitates. On the other hand, Zn seems to have less preference for particular local atomic sites. It can be observed that Zn has a weak preference for a number of sites: such as the Ag and Al sites in the β'Ag phase [19], the Cu sites in the C phase [30] and the Al and Si sites in the U2 phase [8], see Figures 5 and 9. Some Zn is observed in Al fcc sites, as can be seen as an enrichment (of "bright spots") at precipitate/matrix interface in Figure 6. This is probably a consequence of localized high interfacial strain, which could favor the Zn atoms with respect to Al. The observation resembles the case of Ag enrichment of the Al matrix around β'Ag precipitates [19]. It is also observed that the structure of the disordered precipitates contains fragments and/or unit cell of the β" phase, see Figures 5 and 7. Apart from the disordered precipitates, a perfect β" precipitate was also observed, as shown in Figure 8. In the case of the β" precipitate, Zn is only been observed at the Si3/Al sites [2, 3], see Figures 8 and 9. The contrast of these Zn atomic columns is relatively weak although it is higher than intensities of the Si columns, which indicates a low Zn occupancy in the site. It is interesting to note that the Si3/Al site in β" phase is locally identical to the Al site in the U2 phase, as these precipitates show close structural similarities, see Figure 9.

All these observations show that the general effect of Zn on precipitate structure is weak, as no new Zn-containing precipitate types have been observed. In other words, Zn does not alter precipitation sequence in the Al-Mg-Si system. Zn is rather

incorporated into the structures of known precipitates by partly replacing other elements. The overall fraction of Zn in such precipitates is small. A simple calculation assuming 100% Zn occupancy in all Zn-containing columns in the precipitates shown in Figures 5, 7 and 8 (which is never the case based on the Zn-contrast) would set the highest limit of Zn to 18% in β" precipitates, and to 18% and 11% in the disordered precipitates shown in Figures 5 and 7, respectively. Further investigation including quantitative HAADF-STEM, image simulations and first principle calculations will have to be performed for a better estimation of the Zn occupancies in the Zn-containing atomic columns.

4. Conclusions

The effects of Zn additions (up to 1 wt%) on precipitate microstructures, mechanical properties, corrosion properties and precipitate structures in Al-Mg-Si alloys have been investigated as a function of aging at 185°C. It could be concluded that Zn additions up to 0.1 wt% do not have a measurable influence on these properties and parameters. However, a slight increase in materials hardness and a decrease in electrical conductivity have been detected at 1 wt% Zn. The higher hardness correlates with a quantified increase in precipitate number density. The lower electrical conductivity suggests more Zn exists in solid solution. No precipitates of the Al-Zn-Mg system have been detected, instead all investigated areas showed needles parallel to <100>Al, characteristic for the Al-Mg-Si system. Zn segregation along grain boundaries was observed in the peak-aged condition of LZ4. This was found to be linked to high IGC susceptibility. The IGC susceptibility was lower in an under-aged condition. Most precipitates had disordered cross-sections while some β" were also observed. All disordered precipitates were based on the Si-network and incorporated fragments of known metastable phases in the Al-Mg-Si(-Cu) system. Low amounts of Zn have been

observed to enter the structures of all investigated precipitates. However, Zn does not alter precipitation sequence of the Al-Mg-Si system, but makes precipitate disordered. Most Zn-containing atomic columns had low and fluctuating Zn occupancies. These columns occupy positions both in-between the columns of the Si-network, or replacing the Si-network columns. Weak Zn preference for certain atomic sites was found.

References

[1] G.A. Edwards, K. Stiller, G.L. Dunlop and M.J. Couper: *Acta Mater.*, (1998), vol. 46, pp. 3893-3904.

[2] S.J. Andersen, H.W. Zandbergen, J. Jansen, C. Træholt, U. Tundal and O. Reiso: *Acta Mater.*, (1998), vol. 46, pp. 3283-3298.

[3] H.S. Hasting, A.G. Frøseth, S.J. Andersen, R. Vissers, J.C. Walmsley, C.D. Marioara, F. Danoix, W. Lefebvre and R. Holmestad: *J. Appl. Phys.*, (2009), vol. 106, 123527-1-123527-9.

[4] C.D. Marioara, S.J. Andersen, H.W. Zandbergen and R. Holmestad: *Metall. Mater. Trans. A*, (2005), vol. 36, pp. 691-702.

[5] C.D. Marioara, H. Nordmark, S.J. Andersen, H.W. Zandbergen and R. Holmestad: *J. Mater. Sci.*, (2006), vol. 41, pp. 471-478.

[6] R. Vissers, M.A. van Huis, J. Jansen, H.W. Zandbergen, C.D. Marioara and S.J. Andersen: *Acta Mater.*, (2007), vol. 55, pp. 3815-3823.

[7] S. J. Andersen, C.D. Marioara, R. Vissers, A. Frøseth and H.W. Zandbergen, *Mater. Sci. Eng. A*, (2007), vol. 444, pp. 157-169.

[8] S.J. Andersen, C.D. Marioara, A. Frøseth, R. Vissers and H.W. Zandbergen, Mater. Sci. Eng. A 390, (2005), pp. 127-138.

[9] K. Matsuda, Y. Sakaguchi, Y. Miyata, Y. Uetani, T. Sato, A. Kamio and S. Ikeno, *J. Mater.Sci.*, (2000), vol. 35, pp. 179-189.

[10] C.D. Marioara, S.J. Andersen, T.N. Stene, H. Hasting, J. Walmsley, A.T.J. Van Helvoort and R. Holmestad: *Phil. Mag.*, (2007), vol. 87, pp. 3385-3413.

[11] D.J. Chakrabarti and D.E. Laughlin: *Prog. Mater. Sci.*, (2004), vol. 49, pp. 389-410.

[12] C. Cayron, L. Sagalowicz, O. Beffort and P.A. Buffat: *Phil. Mag. A*, (1999), vol. 79, pp. 2833-2851.

[13] K. Matsuda, Y. Uetani, T. Sato and S. Ikeno: *Metall. Mater. Trans. A*, 32 (2001), pp. 1293-1299.

[14] L. Arnberg and B. Aurivillius: *Acta Chem. Scand. A*, (1980), vol. 34, pp. 1-5.

[15] R. Bjørge, C.D. Marioara, S.J. Andersen and R. Holmstad: Metall. Mater. Trans A, 41 (2010), pp. 1907-1916.

[16] R. Bjørge, P.N.H. Nakamura, C.D. Marioara, S.J. Andersen, B.C. Muddle, J. Etheridge and R. Holmstad: *Acta Mater.*, 59 (2011), pp. 6103-6109.

[17] R. Bjørge, S.J. Andersen, C.D. Marioara, J. Etheridge and R. Holmstad: *Philos. Mag*, 92 (2012), pp. 3983-3993.

[18] K. Matsuda, K. Kido, T. Kawabata, Y. Uetani, S. Ikeno: J. Jpn. Inst. Light Met., 53 (2003), pp. 528-533.

[19] C.D. Marioara, J. Nakamura, K. Matsuda, S.J. Andersen, R. Holmestad, T. Sato, T. Kawabata and S. Ikeno: *Philos. Mag*, 92 (2012), 1149-1158.

[20] T. Saito, S. Muraishi, C.D. Marioara, S.J. Andersen, J. Røyset and R. Holmestad: *Metall. Mater. Trans. A*, 44 (2013) 4124-4135.

[21] S. Wenner, C.D. Marioara, S.J. Andersen, R. Holmestad: Mater. Sci. Eng. A, 575 (2013), 241-247.

[22] L.K. Berg, J. Gjønnes, V. Hansen, X.Z. Li, M. Knutson-Wedel, G. Waterloo, D. Schryvers and L.R. Wallenberg: *Acta. Mater.*, 49 (2001), 3443-3451.

[23] G. Sha and A. Cerezo, *Acta. Mater.*, 52 (2004), 4503-4516.

[24] C.D. Marioara, W. Lefebvre, S.J. Andersen, J. Friis, J. Mater. Sci. 48 (2013), 3638-3651.

[25] S.J. Andersen: *Metall. Mater. Trans. A*, 26 (1995), 1931-1938.

[26] P.D. Nellist and S.J. Pennycook: *Ultramicroscopy*, (1999), vol. 78, pp. 111-124.

[27] T. Yamazaki, M. Kawasaki, K. Watanabe, I. Hashimoto and M. Shiojiri: *Ultramicroscopy*, (2002), vol. 92, pp. 181-189.

[28] G. Svenningsen, M.H. Larsen, J.C. Walmsley, J.H. Nordlien and K. Nisancioglu: Corros. Sci. 48, (2006), 1528-1543.

[29] M.H. Larsen, J.C. Walmsley, O. Lunder, R.H. Mathiesen, K- Nisancioglu, J. Electrochem. Soc. 155 (11) (2008), C550-C556.

[30] M. Torsæter, F.J.H. Ehlers, C.D. Marioara, S.J. Andersen and R. Holmestad: *Phil. Mag.* 92 (2012), pp. 3833-3856.

[31] T. Saito, C.D. Marioara, S.J. Andersen, W. Lefebvre and R. Holmestad: *Phil. Mag.* (2013) Accepted DOI:10.1080/14786435.2013.857051

Table 1 Measured alloy compositions (wt%) for the five alloys studied.

Alloys/Elements	Al	Mg	Si	Fe	Zn	Other
LZ0	Bal.	0.47	0.40	0.07	0.000	0.000
LZ1	Bal.	0.48	0.39	0.07	0.002	0.000
LZ2	Bal.	0.47	0.40	0.07	0.012	0.000
LZ3	Bal.	0.48	0.41	0.07	0.110	0.000
LZ4	Bal.	0.47	0.39	0.07	1.019	0.000

Table 2 Precipitate statistics for the LZ1 and LZ4 alloys calculated from a combination of bright-field TEM images and thickness measured by PEELS according to the methodology [4, 25].

	Needle length [nm]	Number density [μm^{-3}]	Cross section [nm^2]	Volume fraction [%]
LZ1	55.43±0.74	6397±663	13.09±0.58	0.46±0.02
LZ4	53.52±0.57	7230±792	12.54±0.57	0.49±0.03
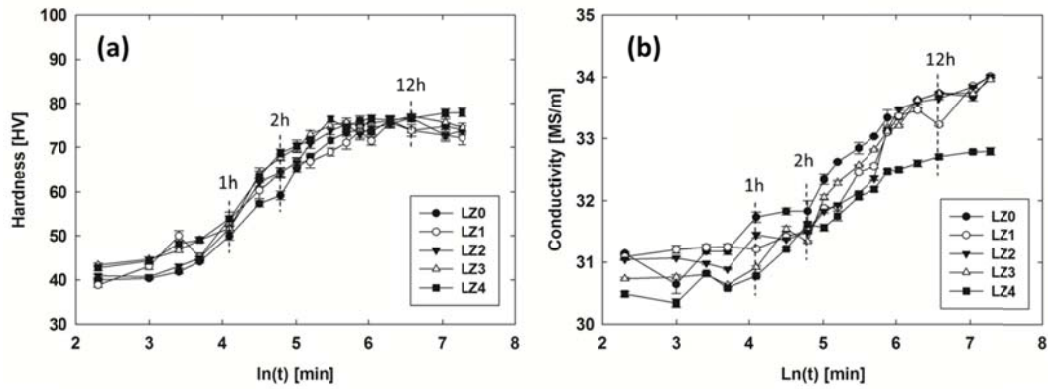
Figure 1 (a) Hardness and (b) electrical conductivity curves for the five Zn-containing alloys during an aging at 185°C. The designations and alloy compositions are shown in Table 1.
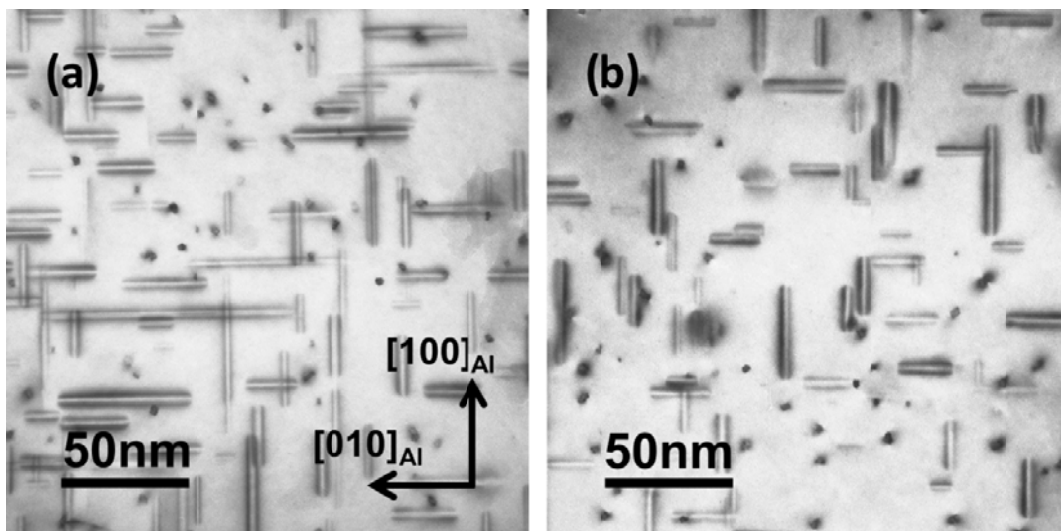
Figure 2 Bright-field TEM images taken along <001>Al directions for (a) LZ1 and (b) LZ4 after an aging at 185°C for 12 hours. For a direct comparison, the images are recorded in areas with similar thickness between 70 nm and 110 nm. Crystallographic orientation for (b) is the same as that for (a). Dark spots represent cross sections of the needle-shaped precipitates along the viewing direction. See Table 2 for corresponding microstructure quantification.
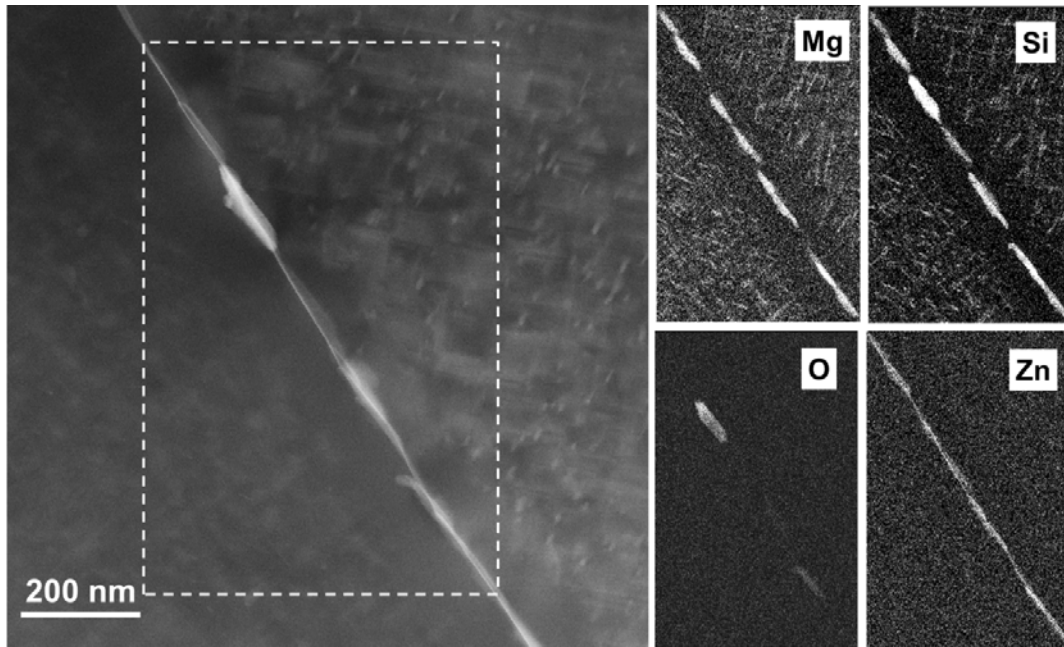
Figure 3 ADF-STEM image (left) for LZ4 after the aging at 185°C for 12 hours and corresponding to EDS elemental maps for relevant elements (right) in the analyzed area delimited by the dashed line rectangle. Alphabetic notations represent Mg: Magnesium, Si: Silicon, O: Oxygen and Zn: Zinc.
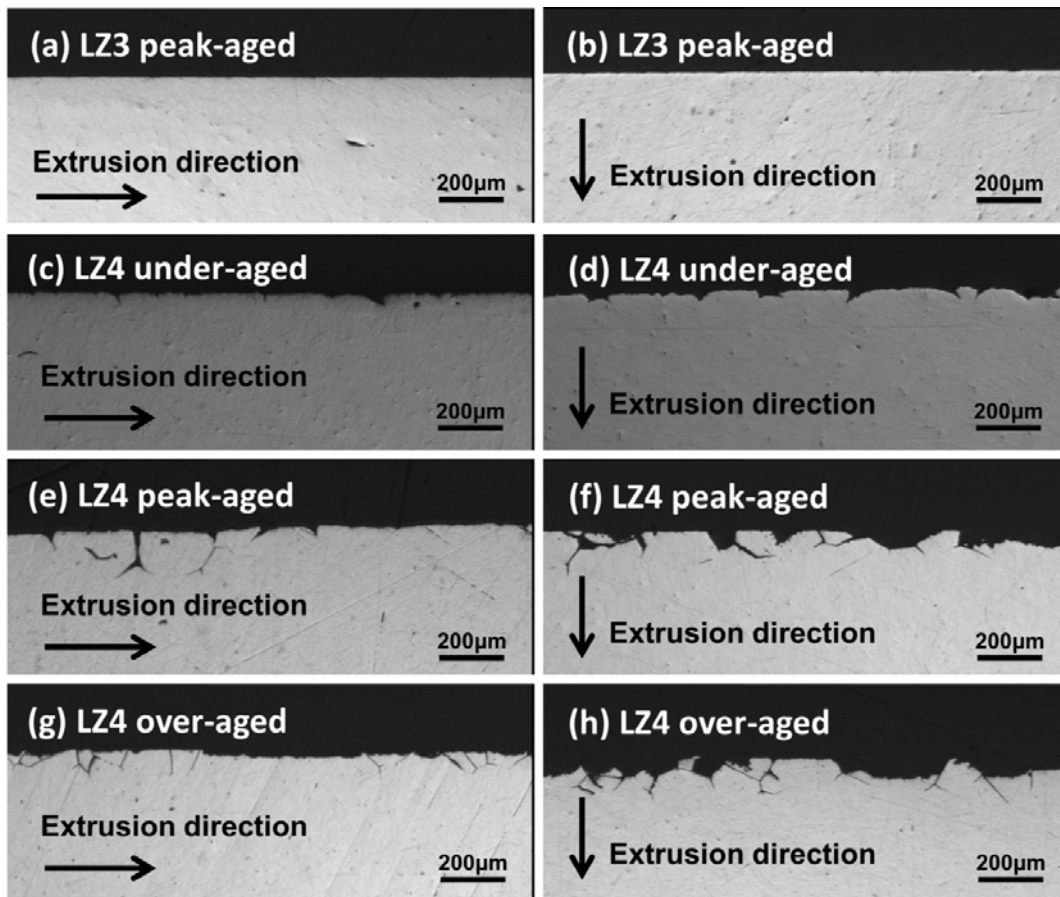
Figure 4 Cross-section optical micrographs after IGC test (a, b) for LZ3 for peak-aged
(2 h), (c, d) for LZ4 for under-aged (2 h), (e, f) for LZ4 for peak-aged (12 h) and (g, h)
for LZ4 for over-aged (30 h) conditions. The surface is either parallel (a, c, e, g) or
perpendicular (b, d, f, h) to the extrusion direction. Cross-section for LZ0, LZ1 and LZ2
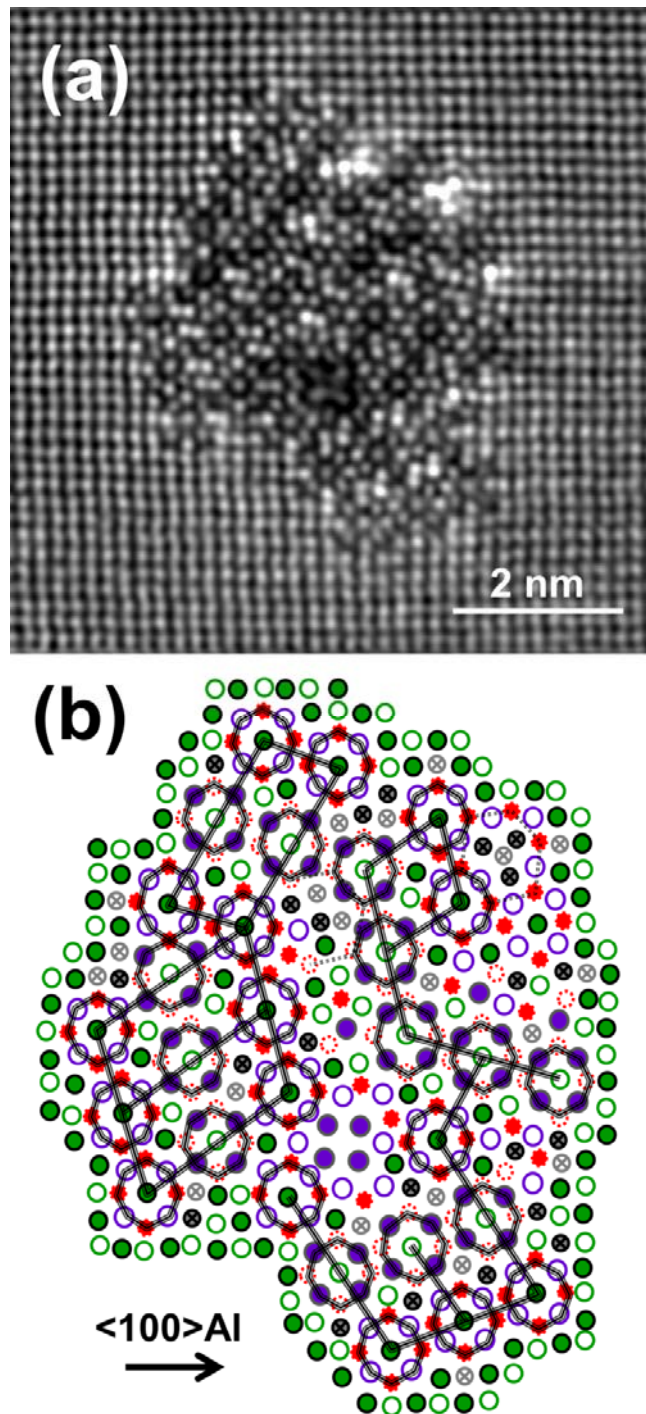(not shown) are similar to that for LZ3.
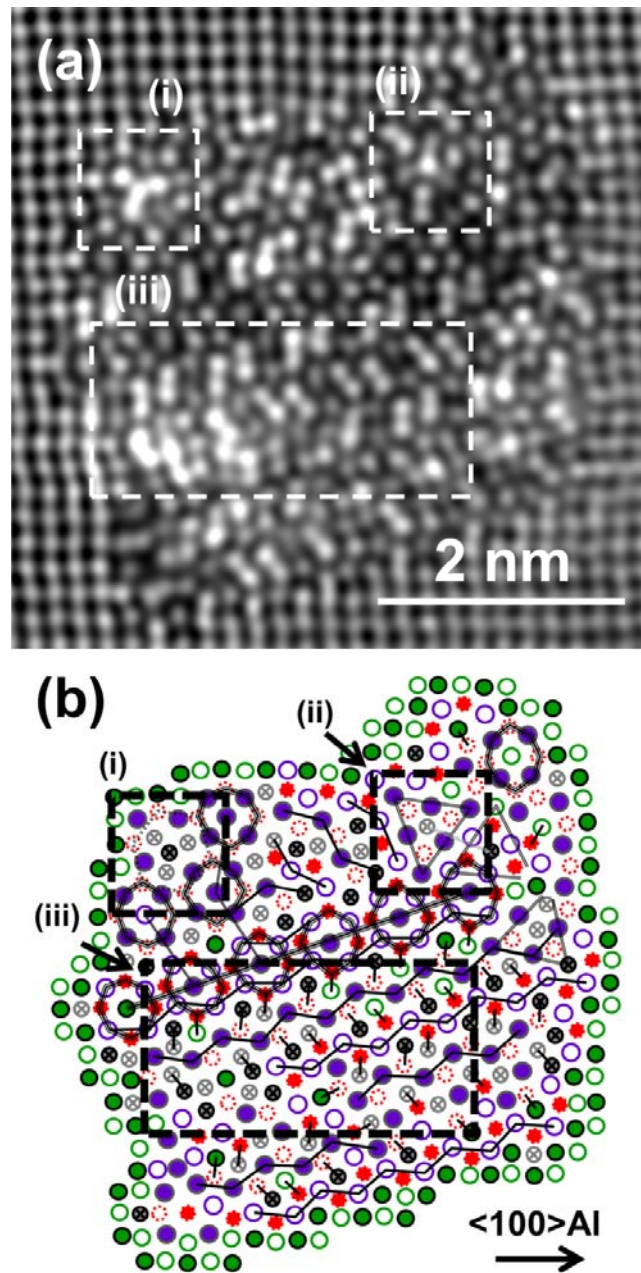
Figure 5 HAADF-STEM images of disordered precipitate cross-section taken along <001>Al for LZ4 after aging for 12 hours. (a) FFT filtered image and (b) suggested atomic overlay. Local atomic configurations shown in the areas (i), (ii) and (iii) can be identified as the β'Ag phase [19], the C phase [30] and the U2 phase [8], respectively. See legend in Figure 9.
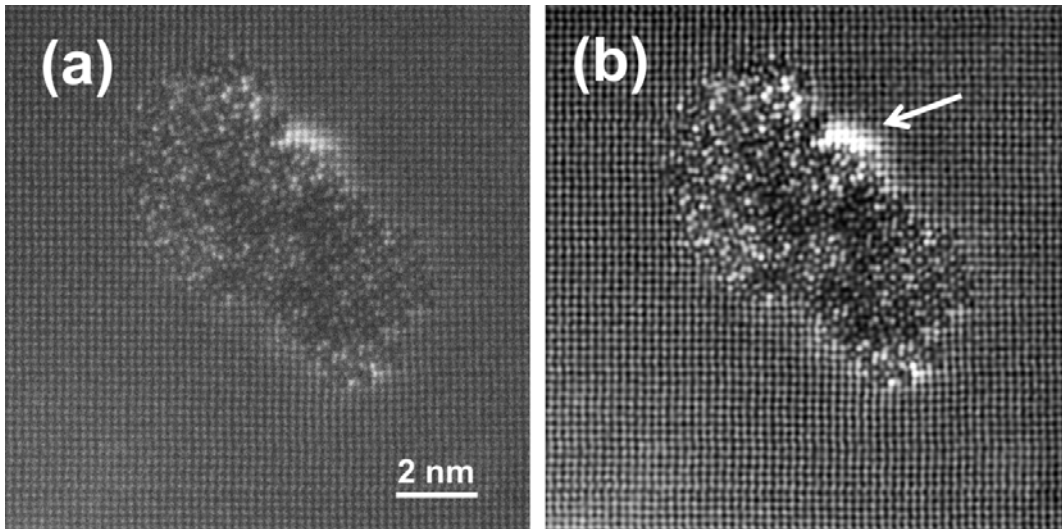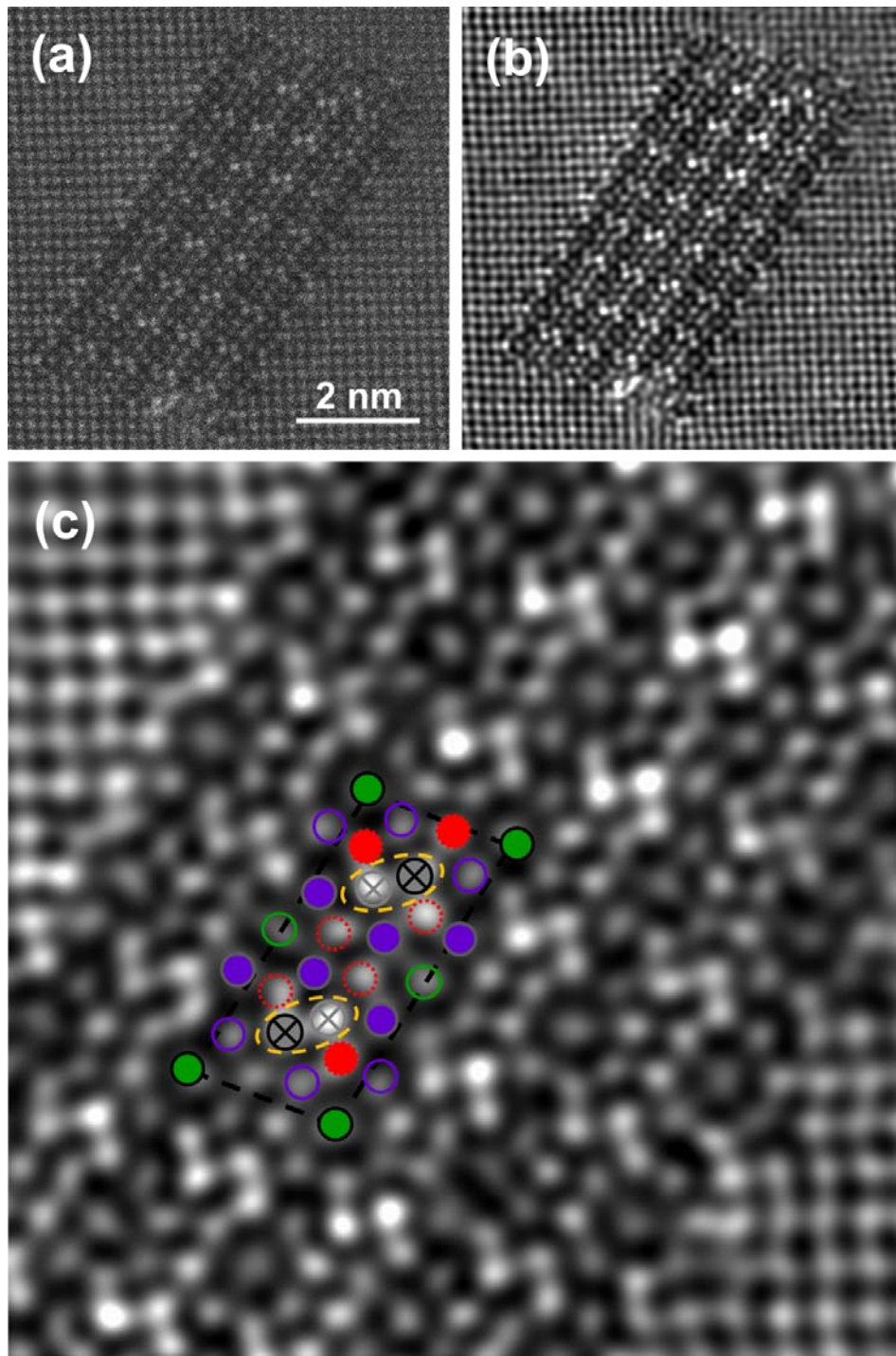
Figure 6 HAADF-STEM images of disordered precipitate cross-section taken along <001>Al for LZ4 after aging for 12 hours. (a) Unprocessed image, (b) FFT filtered image of (a). White solid arrow shows Zn atoms segregated to the interface, but occupying Al fcc positions.

Figure 7 HAADF-STEM images of disordered precipitate cross-section taken along <001>Al for LZ4 after aging for 12 hours. (a) FFT filtered image and (b) suggested atomic overlay on the image (a). See legend in Figure 9.

Figure 8 HAADF-STEM images of a β" precipitate cross-section taken along <001>Al for LZ4 after aging for 12 hours. (a) Unprocessed image, (b) FFT filtered image of (a) and (c) enlarged image of (b) with overlay of a unit cell of the β" phase. See legend in Figure 9.

Elements/Height	Al	Mg	Si	Cu	Ag	Zn
z = 0.000 nm	●	●	✺	●	●	⊗
z = 0.203 nm	○	○	◌	○	○	⊗

＝＝＝＝＝＝＝＝ Ag local symmetry as in β'$_{Ag}$ phase

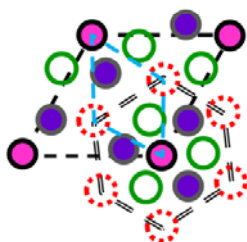══════ Cu local symmetry as in C phase

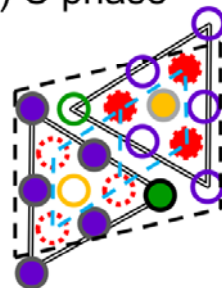────── U2 phase

════ β" phase

⬭ Si3/Al site in β" phase

▬ ▬ ▬ ▬ Si network

(a) β'$_{Ag}$ phase
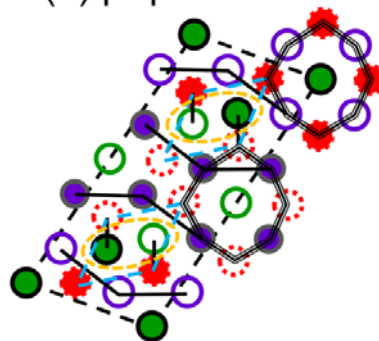
(b) C phase

(c) U2 phase

(d) β" phase

0.675nm

Figure 9 Legend representing atomic overlays in Figures 5, 7 and 8 and schematic drawings of unit cells of the encountered metastable precipitates: (a) the β'Ag phase [19], (b) the C phase [30], (c) the U2 phase [8] and (d) the β" phase with assumed Mg4Al3Si4 composition [2, 3], all drawn to the same scale. Columns containing Zn appear as replacing the Ag and Al atomic columns in the β'Ag phase, the Cu atomic columns in the C phase, the Al and Si atomic columns in the U2 phase and the Al atomic columns in the β" phase, see Figures 5, 7 and 8.